Textbook of *in vivo* Imaging in Vertebrates

Editors

Vasilis Ntziachristos
Department of Radiology, Harvard University HMS/MGH, Charlestown, USA

Anne Leroy-Willig
U2R2M, CNRS and Université Paris-Sud, Orsay, France

Bertrand Tavitian
Unité d'Imagerie de l'Expression des Genes, INSERM, Orsay, France

John Wiley & Sons, Ltd

Textbook of *in vivo* Imaging in Vertebrates

Textbook of *in vivo* Imaging in Vertebrates

Editors

Vasilis Ntziachristos
Department of Radiology, Harvard University HMS/MGH, Charlestown, USA

Anne Leroy-Willig
U2R2M, CNRS and Université Paris-Sud, Orsay, France

Bertrand Tavitian
Unité d'Imagerie de l'Expression des Genes, INSERM, Orsay, France

John Wiley & Sons, Ltd

John Wiley & Sons Ltd, The Atrium, Southern Gate, Chichester,
West Sussex PO19 8SQ, England

Telephone (+44) 1243 779777

Email (for orders and customer service enquiries): cs-books@wiley.co.uk
Visit our Home Page on www.wiley.com

Other Wiley Editorial Offices

John Wiley & Sons Inc., 111 River Street, Hoboken, NJ 07030, USA

Jossey-Bass, 989 Market Street, San Francisco, CA 94103-1741, USA

Wiley-VCH Verlag GmbH, Boschstr. 12, D-69469 Weinheim, Germany

John Wiley & Sons Australia Ltd, 42 McDougall Street, Milton, Queensland 4064, Australia

John Wiley & Sons (Asia) Pte Ltd, 2 Clementi Loop #02-01, Jin Xing Distripark, Singapore 129809

John Wiley & Sons Canada Ltd, 6045 Freemont Blvd, Mississauga, ONT, L5R 4J3, Canada

Wiley also publishes its books in a variety of electronic formats. Some content that appears in print may not be available in electronic books.

Anniversary Logo Design: Richard J. Pacifico

Library of Congress Cataloging-in-Publication Data

Ntziachristos, Vasilis.
Textbook of in vivo imaging in vertebrates / Vasilis Ntziachristos, Anne Leroy-Willig, Bertrand Tavitian.
p. ; cm.
Includes bibliographical references.
ISBN 978-0-470-01528-5 (alk. paper)
1. Diagnostic imaging. 2. Animal models in research. I. Leroy-Willig, Anne. II. Tavitian, Bertrand. III. Title.
[DNLM: 1. Diagnostic Imaging–methods. 2. Animals, Laboratory. 3. Models, Animal. WN 180 N961t 2007]
RC78.7.D53N82 2007
616.07'54–dc22 2007011297

British Library Cataloguing in Publication Data

A catalogue record for this book is available from the British Library

ISBN 978-0-470-01528-5

Typeset in 10/12 pt Sabon by Thomson Digital Noida, India
Printed and bound in Trento, Italy by Printer Trento SRL
This book is printed on acid-free paper responsibly manufactured from sustainable forestry in which at least two trees are planted for each one used for paper production.

Contents

Contributors

Silvio Aime Department of Chemistry IFM and Molecular Imaging Center, University of Torino, Via. P. Giuria 7, I-10125 Turin, Italy
e-mail: silvio.aime@unito.it

Valérie Allamand INSERM U582, Institut de Myologie, Groupe Hospitalier Pitié-Salpétrière, 75651 Paris, France
e-mail: v.allamand@myologie.chups.jussieu.fr

Fred S. Azar Imaging and Visualization, Siemens Corporate Research, Princeton, NJ 08540, USA
e-mail: fred.azar@siemens.com

Daniel Balvay Laboratoire de Recherche en Imagerie, Necker Université Paris V Descartes, Department de Radiologie, Hospital Europeen Georges Pompidou, 75015 Paris, France
e-mail: Daniel.balvay@egp.aphp.fr

Wolfgang R. Bauer Medizinische Universitätsklinik 1, Josef Schneider Strasse 2, D-97080 Würzburg, Germany
e-mail: w.bauer@medizin.uni-wuerzburg.de

Geneviève Berger Laboratoire d'Imagerie Paramétrique, UMR 7623 C.N.R.S.- Université Paris 6, 15 rue de l'Ecole de Médecine, 75006 Paris, France
e-mail: genevieve.berger@lip.bhdc.jussieu.fr

S. Lori Bridal Laboratoire d'Imagerie Paramétrique, UMR 7623 C.N.R.S.-Université Paris 6, 15 rue de l'Ecole de Médecine, 75006 Paris, France
e-mail: bridal@lip.bhdc.jussieu.fr

Edward B. Brown Department of Biomedical Engineering, Box 639 University of Rochester Medical Center, 601 Elmwood Avenue, Rochester, NY, 14642, USA
e-mail: Edward_Brown@URMC.Rochester.edu

Olivier Clement Laboratoire de Recherche en Imagerie, Necker Université Paris V Descartes, Radiology Department Hospital Européen Georges Pompidou, 75015 Paris, France
e-mail: clement@necker.fr

Nora De Clerck Microtomography, University of Antwerp, Department of Biomedical Sciences, Universiteitsplein 1 B-2610 Antwerp, Belgium
e-mail: nora.declerck@ua.ac.be

Christian Combe INSERM E362, Université Victor Segalen-Bordeaux 2, 33076 Bordeaux, France
e-mail: christian.combe@chu-bordeaux.fr

Jean-Michel Correas Laboratoire d'Imagerie Paramétrique, UMR 7623 C.N.R.S.- Université Paris 6, 15 rue de l'Ecole de Médecine, 75006 Paris, France
e-mail: jean-michel.correas@nck.aphp.fr

Charles André Cuénod Laboratoire de Recherche en Imagerie, Necker Université Paris V Descartes, Department de Radiologie, Hospital Europeen Georges Pompidou, 75015 Paris, France
e-mail: charles-andre.cuenod@egp.aphp.fr

Yahsou Delmas ERT CNRS, Imagerie Moléculaire et Fonctionnelle, INSERM E362, Université Victor Segalen-Bordeaux 2,146 rue Léo-Saignat – 33076 Bordeaux, France
e-mail: yahsou.delmas@chu-bordeaux.fr

Rick M. Dijkhuizen Image Sciences Institute, University Medical Center Utrecht, Bolognalaan 50, 3584 CJ Utrecht, The Netherlands
e-mail: rick@invivonmr.uu.nl

Fréderic Dollé Groupe de Radiochimie, Laboratoire d'Imagerie Moléculaire Expérimentale, CEA, Direction des Sciences du Vivant, Institut d'Imagerie Biomédicale Médicale, Service Hospitalier Frédéric Joliot, 4 place du Général Leclerc, 91401 Orsay, France
e-mail: frederic.dolle@cea.fr

Andrew K. Dunn Biomedical Engineering Department, University of Texas at Austin, 1 University Station, C0800, Austin, TX 78712, USA
e-mail: adunn@mail.utexas.edu

Zahi A. Fayad Imaging Science Laboratories, Department of Radiology, Zena and Michael A. Wiener Cardiovascular Institute, Box 1234, One Gustave L. Levy Place, New York, NY 10029, USA
e-mail: Zahi.Fayad@mssm.edu

Danielle Geldwerth-Feniger INSERM U770, Hôpital Kremlin-Bicêtre, 78, rue du General Leclerc 94275, Le Kremlin-Bicêtre, France
e-mail: danielle.geldwerth@kb.inserm.fr

Denis Fize Centre de Recherche Cerveau et Cognition, CNRS-UPS UMR 5549, Université Paul Sabatier, 31062 Toulouse, France
e-mail: Denis.Fize@cerco. ups-tlse.fr

Johann Le Floc'h Department of Electronics, University of Roma Tre, Via della Vasca Navale, 84 00146 Rome, Italy
e-mail: lefloch@uniroma3.it

F. Stuart Foster Department of Medical Biophysics, Ontario Cancer Institute University of Toronto, 610 University Avenue, Toronto M5G 2M9, Canada
e-mail: stuart.foster@swri.ca

Laure Fournier Laboratoire de Recherche en Imagerie, Necker Université Paris V Descartes, Radiology Department, Hospital Européen Georges Pompidou, 75015 Paris, France
e-mail: laure.fournier@egp.aphp.fr

Yves Fromes Inserm U582, Institut de Myologie, Université Pierre et Marie Curie-Paris 6, IFR14, Groupe Hospitalier Paris Saint Joseph, Department of Cardiac Surgery, F-75014 Paris, France
e-mail: y.fromes@myologie.chups.jussieu.fr

Dai Fukumura E. L. Steele Laboratory for Tumor Biology, Department of Radiation Oncology Massachusetts General Hospital, Boston, MA 02114, USA
e-mail: dai@steele.mgh.edu

Urs Giger Section of Medical Genetics, University of Pennsylvania School of Veterinary Medicine, Philadelphia, PA 19104, USA
e-mail: giger@vet.upenn.edu

Nicolas Grenier ERT CNRS, Imagerie Moléculaire et Fonctionnelle, Université Victor Segalen-Bordeaux 2, 146 rue Léo-Saignat - 33076 Bordeaux, France
e-mail: nicolas.grenier@chu-bordeaux.fr

Jan Grimm Laboratory for Bio-optics and Biological Imaging, MGH-CMIR, Building 149 Room 5406, 13th Street, Charlestown, MA 02129-2060, USA
e-mail: jgrimm@helix.mgh.harvard.edu

Jodi Haller Laboratory for Bio-optics and Molecular Imaging, Center of Molecular Imaging Research, Massachusetts General Hospital, Harvard Medical School, Building 149, 13th Street, Room 5406, Charlestown, MA 02129-2060, USA
e-mail: jhaller@partners.org

Philippe Hantraye CEA-UIIBP and URA CEACNRS 2210, Institut d'Imagerie Biomédicale Médicale, Service Hospitalier Frédéric Joliot, 4 place du Général Leclerc, 91401 Orsay, France
e-mail: Philippe.hantraye@cea.fr

Olivier Hauger ERT CNRS, Imagerie Moléculaire et Fonctionnelle, Université Victor Segalen-Bordeaux 2 146 rue Léo-Saignat - 33076 Bordeaux, France
e-mail: olivier.hauger@chu-bordeaux.fr

Vít Herynek MR Unit, Department of Diagnostics and Interventional Radiology, Institute for Clinical and Experimental Medicine, Videnska 1958/9, 140 21 Prague 4, Czech Republic
e-mail: vit.herynek@medicon.cz

Mathias Hoehn In vivo NMR Laboratory, Max Planck Institute for Neurological Research, Center for Molecular Medicine and Department of Neurology, University of Cologne Gleuelerstrasse 50, 50931 Cologne, Germany
e-mail: mathias@mpinkoeln.mpg.de

Andreas H. Jacobs Laboratory for Gene Therapy and Molecular Imaging at the Max Planck Institute for Neurological Research, Center for Molecular Medicine and Department of Neurology, University of Cologne, Gleuelerstrasse 50, 50931 Cologne, Germany
e-mail: Andreas.Jacobs@nf.mpg.de

Russell E. Jacobs Beckman Institute, California Institute of Technology, Pasadena, CA 91125, USA
e-mail: rjacobs@caltech.edu

Rakesh K. Jain E. L. Steele Laboratory for Tumor Biology, Massachusetts General Hospital, Boston, MA 02114, USA
e-mail: jain@steele.mgh.edu

Erwan Jouannot Laboratoire d'Imagerie Parametrique, UMR 7623 C.N.R.S. - Universite Paris 6, 15 rue de l'école de médicine, 75006 Paris, France
e-mail: jouannot@sanofi-aventis.com

Markus Klein Laboratory for Gene Therapy and Molecular Imaging at the Max Planck Institute for Neurological Research, Center for Molecular Medicine and Department of Neurology, University of Cologne Gleuelerstrasse 50, 50931 Cologne, Germany
e-mail: info@nf.mpg.de

Benedict Law Center for Molecular Imaging Research, Massachusetts General Hospital, Harvard Medical School, Charlestown, MA 02129, USA
e-mail: blaw@partners.org

Vincent Lebon CEA-UIIBP and URA CEA-CNRS 2210, Institut d'Imagerie Biomédicale Médicale, Service Hospitalier Frédéric Joliot, 4 place du Général Leclerc, 91401 Orsay, France
e-mail: Vincent.lebon@cea.fr

Anne Leroy-Willig U2R2M (UMR8081 C.N.R.S.), Batiment 220, Université Paris-Sud, Faculté d'Orsay, 91405 Orsay, France
e-mail: anne.leroywillig@u2r2m.u-psud.fr

Huongfeng Li Laboratory for Gene Therapy and Molecular Imaging at the Max Planck Institute for Neurological Research, Center for Molecular Medicine and Department of Neurology, University of Cologne, Gleuelerstrasse 50, 50931 Cologne, Germany
e-mail: info@nf.mpg.de

Annemie Van der Linden Bio-Imaging Lab, Department of Biomedical Sciences Groenenborgerlaan 171, University of Antwerp, 2020 Antwerp, Belgium
e-mail: annemie.vanderlinden@ua.ac.be

Olivier Lucidarme Radiology Department, Pitié-Salpêtriére hospital, 47-83 boulevard de l'Hôpital, 75651 Paris, France
e-mail: Olivier.lucidarme@psl.aphp.fr

Kevin McCully Department of Kinesiology, University of Georgia, Athens, GA 30602, USA
e-mail: mccully@uga.edu

Vincent Van Meir Bio-Imaging Lab, University of Antwerp, Campus Middelheim Groenenborgerlaan 171 2020 Antwerp, Belgium
e-mail: Vincent.vanmeir@ua.ac.be

Michel Modo Centre for the Cellular Basis of Behaviour, The James Black Centre, Kings College London, Institute of Psychiatry, 125 Coldharbour Lane, London SE5 9NU, United Kingdom
e-mail: mike.modo@iop.kcl.ac.uk

Xavier Montet Geneva University Hospital, Radiology Department, Rue Micheli-du-Crest 24, 1205 Geneva, Switzerland
e-mail: xavier.montet@hcuge.ch

Willem J.M. Mulder Biomedical NMR, Eindhoven University of Technology, PO Box 513, Eindhoven 5600 MB, The Netherlands
e-mail: w.j.m.mulder@tue.nl

Lance L. Munn E. L. Steele Laboratory for Tumor Biology, Massachusetts General Hospital, Boston, MA 02114, USA
e-mail: lance@steele.mgh.harvard.edu

Matthias Nahrendorf Center for Molecular Imaging Research, Massachusetts General Hospital, Harvard Medical School, Room 5406, 149 13th Street, Charlestown, MA 02129, USA
e-mail: MNahrendorf@partners.org

Koen Nelissen Laboratorium voor Neuro- en Psychofysiologie, K.U.Leuven Medical School, Campus Gasthuisberg Herestraat 49, B-3000 Leuven, Belgium
e-mail: Koen.Nelissen@med.kuleuven.be

Klaas Nicolay Biomedical NMR, Eindhoven University of Technology, PO Box 513, Eindhoven 5600 MB, The Netherlands
e-mail: k.nicolay@tue.nl

Vasilis Ntziachristos Laboratory for Bio-optics and Molecular Imaging, Center of Molecular Imaging Research, Massachusetts General Hospital, Harvard Medical School, Building 149, 13th Street, Room 5406, Charlestown, MA 02129-2060, USA
e-mail: vasilis@helix.mgh.harvard.edu

Guy A. Orban Laboratorium voor Neuro- en Psychofysiologie, K.U.Leuven Medical School, Campus Gasthuisberg, Herestraat 49 B-3000 Leuven, Belgium.
e-mail: Guy.Orban@med.kuleuven.be

Cyrus Papan Institute of Bioengineering and Nanotechnology, The Nanos #04-01, 31 Biopolis Way, Singapore 138669
e-mail: cpapan@ibn.a-star.edu.sg

Roberto Pasqualini Research and Development, CIS bio international, Schering BP 32, 91192 Gif sur Yvette, France
e-mail: Rpasqualini@cisbiointernational.fr

Andrei Postnov Microtomography, Department of Biomedical Sciences, University of Antwerp, Universiteitsplein 1, B-2610 Antwerp, Belgium
e-mail: andrei.postnov@ua.ac.be

Clement Pradel Laboratoire de Recherche en Imagerie, Necker Université Paris V Descartes, Department de Radiologie, Hospital Europeen Georges Pompidou, 75015 Paris, France
e-mail: clement.pradel.@egp.aphp.fr

Laurent Salomon Laboratoire de Recherche en Imagerie, Université Paris V Descartes, Radiology Department, Hospital Européen Georges Pompidou, 75015 Paris, France
e-mail: Laurent.salomon@egp.aphp.fr

Marco Salvatore Dipartimento di Scienze Biomorfologiche e Funzionali, Universita' Federico II, Vias S Pansini 5, 80131 Naples, Italy
e-mail: marco.salvatore@unina.it

Eyk Schellenberger Department of Radiology, Institut für Radiologie, Charité-Universitätsmedizin Berlin, Campus Charité Mitte, Schumannstrasse 20/21, 10117 Berlin, Germany
e-mail: eyk.schellenberger@charite.de

James Sharpe ICREA Research Professor, EMBL/CRG Systems Biology Unit, Centre for Genomic Regulation (CRG), Dr. Aiguader 88, 08003 Barcelona, Spain
e-mail: James.Sharpe@crg.es

Nathalie Siauve Laboratoire de Recherche en Imagerie, Necker Université Paris V Descartes, Radiology Department, Hospital Europeen Georges Pompidou, 75015 Paris, France
e-mail: siauve@necker.fr

Antoine Soubret Novartis Pharma A.G., Modeling & Simulation Biology, WSJ-27.1.026, CH-4056 Basel, Switzerland
e-mail: soubreta@yahoo.fr

Jörg. U.G. Streif Physikalisches Institut, Lehrstuhl für Experimentelle Physik V (Biophysik), Universität Wüerzburg, Am Hubland, 97094 Wüerzburg, Germany
e-mail: streif@physik.uni-wuerzburg.de

Gustav J. Strijkers Biomedical NMR, Eindhoven University of Technology, PO Box 513, Eindhoven 5600 MB, The Netherlands
e-mail: g.j.strijkers@tue.nl

Bertrand Tavitian INSERM U803, Imagerie de l'expression des gènes, Laboratoire d'Imagerie Moléculaire Expérimentale, CEA, Direction des Sciences du Vivant, Institut d'Imagerie Biomédicale Médicale, Service Hospitalier Frédéric Joliot, 4 place du Général Leclerc, 91401 Orsay, France
e-mail: bertrand.tavitian@cea.fr

Régine Trébossen Groupe Instrumentation et Traitement d'Images, Laboratoire d'Imagerie Moléculaire Expérimentale, CEA, Direction des Sciences du Vivant, Institut d'Imagerie Biomédicale Médicale, Service Hospitalier Frédéric Joliot, 4 place du Général Leclerc, 91401 Orsay, France
e-mail: regine.trebossen@cea.fr

Ching-Hsuan Tung Center of Molecular Imaging Research, Massachusetts General Hospital, Harvard Medical School, 149 13th Street, Room 5406, Charlestown, MA 02129, USA
e-mail: tung@helix.mgh.harvard.edu

Wim Vanduffel Massachusetts General Hospital, Massachusetts Institute of Technology, Harvard Medical School, Athinoula A. Martino's Center for Biomedical Imaging, Charlestown, MA 02129, USA
e-mail: wim@nmr.mgh.harvard.edu

Greet Vanhoutte Bio-Imaging lab, Campus Middelheim Grenenborgerlaan 171 University of Antwerp, 2020 Antwerp, Belgium
e-mail: greetje.vanhoutte@ua.ac.be

Silvana Del Vecchio Instituto di Biostrutture e Bioimmagini, Consiglio Nazionale delle Ricerche, Universita' Federico II, Via S. Pansini 5, 80131 Naples, Italy
e-mail: delvecc@unina.it

Yannic Waerzeggers Laboratory for Gene Therapy and Molecular Imaging, Max Planck Institute for Neurological Research, Center for Molecular Medicine (CMMC) and Department of Neurology, University of Cologne, Gleuelerstrasse 50, 50931 Cologne, Germany
e-mail: info@nf.mpg.de

Ralph Weissleder Center for Molecular Imaging Research, Massachusetts General Hospital, Harvard Medical School, Room 5406, 149 13th Street Charlestown, MA 02129, USA
e-mail: weissleder@helix.mgh.harvard.edu

Andreas Wunder Molecular Imaging Group, Experimental Neurology, Charité Hospital, Schumannstrasse 20/21, 10098 Berlin, Germany
e-mail: andreas.wunder@charite.de

Jet P. van der Zijden Image Sciences Institute, University Medical Center Utrecht, Bolognalaan 50, 3584 CJ Utrecht, The Netherlands
e-mail: sjet@invivonmr.uu.nl

Introduction

Traditional biomedical methods study ''life'' on dead specimens. To address limitations of in-vitro assays, in-vivo imaging of vertebrates has emerged as a powerful tool used in virtually all forms of modern biomedical research and drug discovery. In-vivo imaging fulfils a basic necessity to dynamically and spatially resolve anatomical, functional and molecular events as they occur in live tissues. How would we quantify the cardiac function and adaptation to a stimulus other than in a live animal? How can the effects of a sensory stimulus on the cerebral cortex be accurately described if not by using in-vivo observations? Similar motivations arise in many other aspects of the life sciences such as examining complex molecular pathways in disease evolution or the longitudinal assessment of treatment.

Following this fundamental requirement for in-vivo assessment of tissue characteristics in the biomedical sciences, significant progress has been made towards non-invasive imaging of animals, from the embryonic stage to fully developed adult stage. This progress has seen three major traits. One approach has been the adaptation of clinical imaging methods to the animal dimensions for obtaining optimal imaging characteristics in the smaller volumes examined. A second trait has been the evolution or development of new methods, primarily based on photonic technologies, which are well suited for small animal research. The third trait has been the engineering of important new chemistry and biotechnology methods that impart significant ability to identify and report on a magnitude of cellular and sub-cellular functions, a capacity that was previously unavailable to traditional medical imaging. These newer imaging technologies have opened the possibility for visualizing proteins, genes and their function in entire animals in-vivo and non-invasively. Imaging of entire intact animals has therefore emerged as one of the important biomedical tools in the post genomic era. Similarly to the significant gains seen by the introduction of the microscope in biology, imaging of entire intact animals enables unprecedented insights at the system level and offers new found capabilities of accurate visualization of structure, physiology and molecular function.

The fundamental principles of interaction and image formation differ significantly between the imaging modalities used in vertebrate imaging. Combined with elaborate methods of inducing biological contrast, the plurality of technologies and the diverse performance characteristics may at times appear daunting not only for the biologist but even for the medical imaging specialist. This book intends to summarize the wealth of imaging technologies and applications that have emerged for in vivo imaging of animals and to serve as a reference to the biologist and biomedical investigator. It serves the dual role of 1) describing the basic underlying principles of image formation using different energies of the electromagnetic radiation spectrum and acoustic waves and of 2) exemplifying representative applications in studying living vertebrates, with the exception of humans. The ultimate goal is to explain the different types of information gained by modern in vivo imaging techniques and illustrate the potential to replace the accurate but destructive histological techniques with high-throughput imaging strategies. The utility of multimodality imaging is also scrutinized as it allows for optimal combination of complementary tissue parameters measured on the same animal/organ and position. Key characteristics and limitations of the different imaging approaches including the specificity and the sensitivity achieved in retrieving various biomarkers, the speed of acquisition for dynamic measurements, the easiness of ''bench-top'' or ''cageside'' application and the appropriateness by which to examine key biological problems is also presented. Minimally invasive imaging modalities increasingly used in biomedical research are also described. By combining expert descriptions of the most widespread imaging approaches for vertebrate imaging, we hope that this book will contribute in collectively describing the most important of imaging approaches in order to categorize them and describe in a concise manner.

Accelerating biomedical discovery

By enabling longitudinal studies, non-invasive imaging comes with increased observation accuracy; each animal can serve as its own control, thus reducing the sources of experimental variability. Moreover, since a single animal yields observations at multiple time points, smaller animal numbers are required in order to build meaningful statistics. This practice overall reduces research cost and the time required to reach meaningful conclusions. With this capacity, animal imaging can significantly accelerate biomedical discovery by enabling expeditious tests of agents, drugs and hypotheses. Imaging can be pivotal for example in accelerating drug discovery or the identification of potent diagnostic agents by utilising the animal as the test bed in the pre-clinical in-vivo assessment of treatment efficiency, targeting sensitivity and specificity, biodistribution and long term effects. Correspondingly, in-vivo imaging is in par with modern legislation that wisely incites researchers to spare animal life. The rule of the three R's – replacement, reduction and refinement of animal experimentation – enounced by Russel and Burch in 1959 is at best respected when atraumatic experimentation is exercised.

Similar benefits can be found when imaging the rising numbers of genetically modified animals, mostly mice, which come with the need for quick screen for phenotypes that correspond to human disease. Transgenic, knock out and knock in techniques can yield a significant number of animal model variants of unknown disease traits. Imaging plays an important role in identifying and comparing different phenotypes to human disease and can accelerate the traditional observations of biochemical testing, physiological inspection and molecular analyses.

In-vivo imaging of animals can further serve as a common framework for animal and human observations and yield a bridge between traditional biomedical research and improving human health. This can be achieved at many different levels. Technologies developed for the assessment of drugs in mice can be translated to imaging efficacy in humans as well, utilizing the imaging experience gained from animal imaging. Similarly, some of the most potent detection technologies, tested in mice, can be then employed diagnostically in humans using the same imaging modality. With modern imaging serving as the common denominator, quick pre-clinical screens and accurate clinical evaluations at the structural, physiological and molecular levels can be facilitated efficiently and at no significant additional technological expense.

Image formation and contrast mechanisms

All modalities used for in-vivo imaging utilize some wave form which non-destructively interacts with tissue. Information on the internal characteristics of tissues is obtained by recording the response to this interaction and is then utilized in forming images. Most imaging modalities use a part of the electromagnetic spectrum to form images, with the exception of ultrasound that uses acousto-mechanical waves. The most typical distinction of different imaging methods, is by means of the particular electromagnetic energy used. Shown in Fig. 1 is the correspondence of the most common imaging methods with the electromagnetic spectrum. The particular physical parameters of the wave used are ultimately responsible for the particular characteristics of each technology. There are three major types of information that can be assessed with modern imaging methods as summarized in Fig. 2:

Anatomical imaging is the traditional radiological approach, largely facilitated by X-ray imaging, X-ray CT, Magnetic Resonance Imaging, Ultrasound and

Figure 1 Wavelength, energy of photon and frequency of electromagnetic radiations used for *in vivo* imaging
Energy of electromagnetic radiation is indicated by the energy of one photon,

$$E = h.F = h.c/\lambda.$$

where h is the Planck's constant equal to 6.62 10^{-23} Joule s, F is the frequency of the wave and λ is its wavelength.
Here E is plotted in eV. Photons with energy higher than 1 eV can ionise molecules and then have biological effects

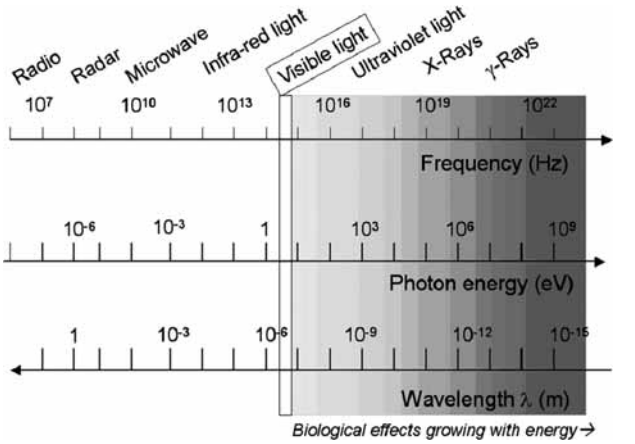

Figure 2 Which kind of information may be-given by the main imaging techniques

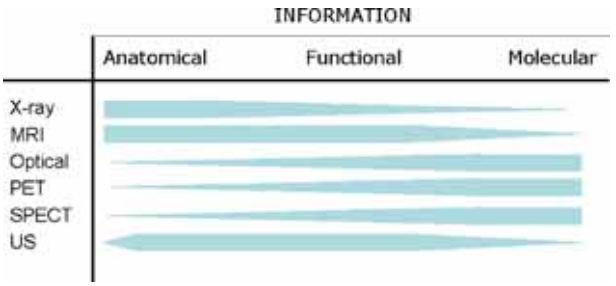

Optical Imaging, the latter when superficial structures are considered. Generally, the information and contrast visualized and the corresponding information conveyed by the image can be found in an anatomy textbook. This anatomical information, or the changes found from the expected known anatomy, relate to development and disease. Typically, these are high resolution images and the contrast imaged is endogenous, i.e. the attenuation of X-ray beams by bone or cancer-related calcifications or the differences between the concentration and motility of water molecules by MRI. However the use of contrast agents is occasionally used to improve the contrast in anatomical structures, for example in resolving the structure of the vascular system or better visualizing a suspicious lesion.

Functional imaging is used to study the function of organs, under physiological or pharmacological stimulations. It typically requires fast measurement techniques and resolves contrast parameters found in your physiology book. It can visualize for example organ movement, fluid flow, membrane permeability and the function of tissue bio-molecules associated with basic tissue function such as haemoglobin or oxygen. Imaging is based either on endogenous contrast or the administration of exogenous agents. All imaging modalities have been used for functional imaging with varying resolutions, often using a high-resolution anatomical image as reference. Examples of functional imaging include the visualization of deoxy haemoglobin changes during functional cortex studies by MRI or optical methods or blood flow measurement during the cardiac cycle by MRI or ultrasound.

Molecular imaging is the most recent of the imaging sciences and it refers to the visualization of biological processes at the cellular and molecular level. Molecular imaging is based on the combination of advanced chemistries, transgenic strategies and imaging technologies in order to resolve engineered contrast specific to particular cellular and sub-cellular processes. Generally it is used to visualize processes found in a molecular biology book and associated fields of science and offers the widest versatility over the two previous methods in terms of the contrast mechanisms that can be achieved and the technologies utilized. The images are typically low resolution and a high-resolution anatomical or functional image is used for reference. Typically all the standard radiological imaging modalities have been used for molecular imaging, except X-ray CT, that does not up to this point offer sufficient sensitivity.

The classification of anatomical, functional and molecular imaging is often associated with particular contrast mechanisms and strategies, but it does not impose strict boundaries. Anatomical imaging for example can be performed after administration of a contrast agent that can better outline architectural features. Similarly, molecular imaging can operate in the absence of exogenous contrast enhanced strategies; for example Magnetic Resonance spectroscopic imaging resolves the relative concentrations of various intrinsic molecules and correspondingly relays information on tissue and disease molecular status, at the absence of extrinsic contrast agents. However, while endogenous contrast can be used as a biomarker in many applications, it is the use of versatile exogenous contrast strategies that brings a new paradigm into animal imaging. There are several different classes of enhancing or generating contrast associated with particular tissue function and molecular activity. The classical approach follows the clinical radiological paradigm where a contrast agent is intravenously injected to enhance the capacity to detect disease. This agent preferentially distributes at the site of interest, or demarcates the vascular structure of an organ of interest. Examples include the injection of an iodinated agent or a super-paramagnetic contrast agent for imparting contrast on X-ray CT or MR images respectively. Another example is the injection of common molecules labeled with radioactive isotopes, or the use of labeled moieties such as antibodies or peptides. This latter approach is a change in paradigm as contrast is in this case engineered for specific biomolecules. This basic example of engineered contrast is significantly augmented in molecular imaging by sophisticated techniques that can mark virtually any protein, an increasingly large number of diverse cellular functions and cell traffic. Collectively, these engineered technologies are referred to as reporter technologies, since they report on specific targets and functions. There are two fundamental reporter approaches, i.e. direct and indirect imaging.

Direct imaging uses exogenously administered probes that are engineered to report on specific

molecular process (e.g., a receptor target imaged with a ligand molecular imaging probe). This approach is similar to the nuclear imaging example discussed in the previous paragraph, but is significantly enhanced for use with different modalities (i.e optical, MRI etc) and using different design principles. Importantly, engineered probes used for direct imaging can be categorized to active probes, i.e. probes that carry an active reporting component and activatable probes, which carry an inactive reporting component which is activated through interaction with a molecular target, or more generally changes some of its own physical parameters after interaction with a specific target. Activatable probes are also known as molecular beacons, switches or smart probes and they are so far available for fluorescence, bioluminescence and MRI. An important distinction of probes vs. contrast agents is that the former have specificity against a gene or gene-expression product.

Indirect imaging refers to methods that utilize a reporter trans-gene which is inserted in the animal's DNA. Contrast is generated after transcription of the reporter gene. The product of the transcription and translation can be a reporter probe directly (for example a fluorescent protein) or otherwise a functional cellular change that facilitates preferential uptake of an exogenously administered probe, for example upregulation of an enzyme or receptor that is in turn responsible for accumulating or trapping a radionuclei-based agent into a cell or the cellular surface. Reporter gene imaging is a generalizable platform that in contrast to the direct imaging method, only one or few well validated reporter-gene & reporter probe pairs can be used to image many different molecular and genetic processes. On the downside is the introduction of foreign proteins and genes which limits applicability to animals.

Chapters

This book is divided into three parts.

The first part presents the basic principles of operation of the most common imaging techniques used in small animal imaging. Chapter 1 is devoted to Nuclear Magnetic Resonance Imaging (and Spectroscopy); Chapter 2 to X-Ray Tomography, Chapter 3 to Ultrasound Imaging. Chapter 4 is devoted to Nuclear Imaging (PET and SPECT) and to the production of radioactive tracers. Chapter 5 is devoted to Optical Imaging, and Chapter 6 to in vivo Optical Microscopy. Chapter 7 shows the newest radioactive tracers, reporters and contrast agents that are proposed in each imaging domain, and Chapter 8 presents the potentialities offered by the combination of several imaging techniques.

The second part is made from reports that each show how a given technique optimally adresses a specific biological question, with four chapters showing illustrations related respectively to brain (Chapter 9), heart vessels and muscle (Chapter 10), tumours (Chapter 11), other organs (Chapter 12).

The third part is devoted to the review of two domains where in vivo imaging has brought new insights: Gene therapies (Chapter 13) and cellular therapies (Chapter 14).

Vasilis Ntziachristos
Anne Leroy-Willig
Bertrand Tavitian

1 Nuclear Magnetic Resonance Imaging and Spectroscopy

Anne Leroy-Willig and
Danielle Geldwerth-Feniger

1.0 Introduction

Nuclear magnetic resonance (NMR) detects the magnetic moments of nuclei using their orientation in a strong magnetic field and their response at a specific resonance frequency. Discovered in 1946 by Bloch and Purcell, NMR spectroscopy (MRS), at first used for chemical and physical studies, quickly became a major tool for spectroscopic analysis of complex molecules and further of biochemical systems. Then in the 1980s, NMR gave rise to magnetic resonance imaging (MRI), a medical imaging technique very attractive despite its cost, from the profusion of anatomical and physiological information available.

In biomedical research, the two modalities, imaging (MRI) and spectroscopy (MRS) are increasingly used for *in vivo* animal studies, with benefit from the technical developments carried out for human studies. These two modalities give access to various data ranging from three dimentional (3D) anatomy to physiological and biochemical information, and many applications are available via specific measurement techniques that we will shortly explain here.

NMR is fully based upon quantum physics. Here we give a simplified and then by some ways approximate description, mixing classic and quantum physics, in paragraphs one to six; the later paragraphs are oriented towards *in vivo* explorations.

In this chapter, several levels of information are given, which are as follows: readers can jump the paragraphs labelled as 'more physics' or 'more technology'; also they may read only key points before coming to the following paragraph. For those who wish to know more about MRI and MRS, more complete descriptions are given in a free access Web book (Hornack, 2005), in books by Webb (2003) and Bushberg *et al.* (2001), and concerning the toolbox of MRI sequences, in Ness Aiver (1997) with a fully graphic presentation. Gadian (1995) wrote an excellent introduction to *in vivo* MRS.

1.1 Magnets and magnetic field

In everyday life, a magnet is a piece of a material which attracts or repels another magnet and creates a magnetic field. For example, the magnetic bar shown in Figure 1.1.1(a) has two poles; the magnetic field it creates goes from the North Pole to the South Pole. The magnetic field all around this magnet can be probed by its action, which is the force exerted on another magnet. For example, the weak earth's magnetic field acts upon a needle compass: The compass rotates and lines along the magnetic field pointing towards the magnetic North.

Magnetism is the fundamental property of matter. The magnetism of nuclei is weak, hidden behind the stronger contribution of electrons, and one may easily ignore its existence. Magnetism is the result of moving electrical charges (mostly the electrons). The magnetic field, the mediator of magnetic force, is created either by electric current flowing in a wire or by the microscopic electric circuits, which exist inside materials like iron, at the atomic scale.

Figure 1.1.1 How to create a magnetic field.
(a) The magnet bar, a rod made with iron, is a permanent source of magnetic field throughout space. The field lines (black curves), that indicate the direction of the magnetic field, go from North Pole to South Pole. A small needle compass lines along the direction of the magnetic field.
(b) A loop of copper wire, fed with electrical current, creates a magnetic field with similar spatial distribution at long distance as indicated by field lines.
(c) A solenoidal winding is made by many conductive wire loops winded upon a cylinder. In the central part of the cylinder, the magnetic field is lined along the axis of the cylinder (white lines) and is homogeneous

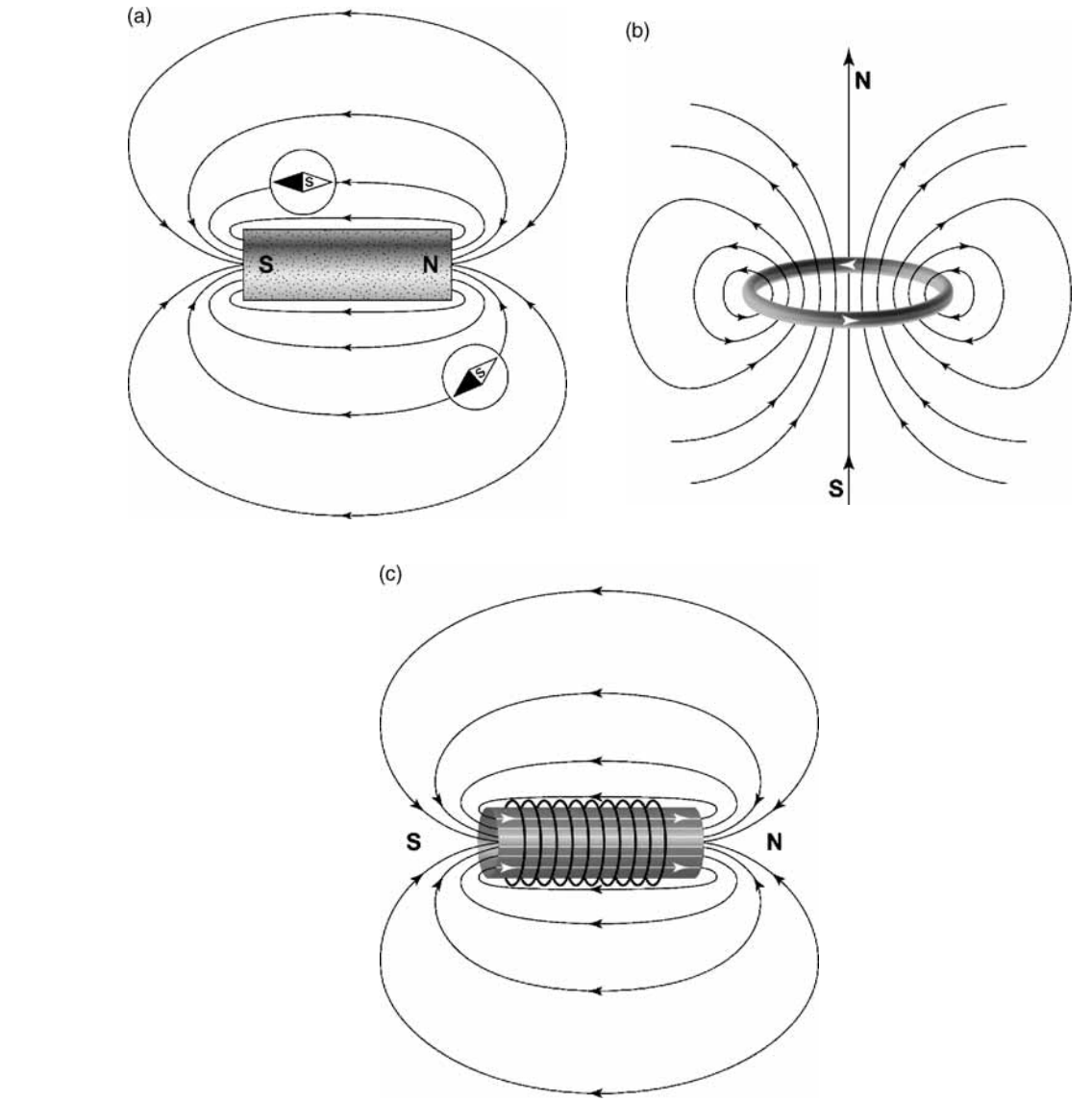

The magnetic field is measured in Tesla or in Gauss, with $1\,\mathrm{T} = 10^4\,\mathrm{G}$. (Note that we make a rather loose use of magnetic units, forgetting the difference between magnetic field and magnetic induction, only needed when studying ferromagnetic materials.)

Another simple magnet is made by a circular loop of copper wire fed with electric current, shown in Figure 1.1.1(b). A basic physical law tells us that the magnetic field created by a current rotates around the wire where the electric current is flowing. Then the magnetic field is perpendicular to the circle at its centre; elsewhere its intensity and its direction vary through space. The solenoid is made with multiple loops of wire coiled upon a cylinder (Figure 1.1.1(c)). The magnetic field inside the cylinder is very homogeneous.

1.1.1 More technology: The 'perpetual' magnet

Nearly all magnets for NMR are solenoids, made of supraconductive wire winded upon a hollow cylindrical support. Electric current circulates in the circuit that is immersed in a cryostat filled with liquid helium at temperature −269°C. Since the supraconductive wire has zero electrical resistance at low temperature, no electrical power is dissipated. This system creates a very stable magnetic field that may be disconnected from a power supply, as long as the temperature is kept low enough. The low temperature is maintained by high vacuum insulation that reduces liquid helium boil off.

Besides the high intensity, high homogeneity and stability of the magnetic field are also needed. The magnet is the more heavy and expensive piece of NMR hardware. There is a growing demand for high field magnets dedicated to biomedical research, but few centres can buy very high field magnets for large animals.

Big magnets delivering magnetic fields between 0.3 and 3 T are currently used for NMR human studies. For smaller animals, smaller magnets delivering higher fields (1.5 to 11 T) are currently used. In vitro experiments are done at still higher fields. For comparison, the earth magnetic field is 5×10^{-4} T (or 0.5 G).

Magnets for small animals are either vertical (as those commonly used for in vitro studies) or horizontal, yielding wider access and allowing more physiological housing of animals during NMR examination (as shown by Figure 1.1.2).

Figure 1.1.2 The supraconductive magnet used for NMR experiments. (a) High field supraconductive magnet for rats and mice NMR examination. This horizontal magnet, weighting 2 tons, delivers a magnetic field of 7 T inside a cylindrical access 30 cm wide. After installation of the shim and gradient coils, the access available for small animals is 15 cm wide. The chimney above the magnet is used for liquid helium refill. (b) Examination bed. The small animal is lain inside an anaesthesia chamber. The bed is positioned at the centre of the magnet bore during the examination (Courtesy of Bruker, SA, Ettlingen, Germany)

1.2 Nuclear magnetization

1.2.1 The magnetic moment of the nucleus

Key points
The nuclei that bear a net magnetic moment (such as ^{1}H, ^{31}P, ^{13}C) can be detected by NMR. Hydrogen nuclei, that bear the largest magnetic moment amongst stable nuclei, are detected to build in vivo NMR images. Hydrogen, phosphorus, sodium, fluorine nuclei are currently detected to build in vivo NMR spectra.

All elementary particles (electron, proton, neutron and others) bear a spin. The spin is purely quantic without strict correspondence in classical physics, but it can be described as a quantity of rotation of the particle spinning about one axis, where each spin $\vec{s}$ is associated with an elementary magnetic moment $\vec{\mu}$, related to the spin by a number, the gyromagnetic factor γ.

$$\vec{\mu} = \gamma . \vec{s} \qquad (1.1)$$

The elementary magnetic moment may be described as a tiny magnet that we will represent as an arrow; a more accurate description is possible only by quantum mechanics, out of our scope.

The spin is the kinetic moment of the particle (a 'quantity of rotation'), and the magnetic moment is always associated – and proportional – to this kinetic moment. (Note that in many books, the word ''spin'' is written instead of 'magnetic moment'.)

For one given nucleus, the magnetic moment is the sum of the magnetic moments of its protons and its neutrons. Hydrogen nucleus is made of one proton (Figure 1.2.1). When protons or neutrons are associated as pairs with their magnetic moments in opposed direction, these pairs have a net magnetic moment equal to zero. For example, the carbon nucleus ^{12}C (with 6 protons and 6 neutrons) cannot be detected by NMR, whereas the less abundant isotope ^{13}C (6 protons, 7 neutrons) has a detectable magnetic moment. In vivo NMR spectroscopy of ^{13}C allows the quantification of molecules such as glucose, acetate and glycogen.

Electrons bear a much larger elementary magnetic moment, nearly two thousand times bigger than that of protons. In most molecules, electrons are associated as pairs with their magnetic moments in opposed direction, and these pairs have nearly net zero magnetic moment. The iron atom has several non-paired electrons and then bears a large magnetic moment from its electrons, so that iron is a good material to experience what is magnetism, or to make magnets, and also NMR contrast agents (see paragraph 1.9).

1.2.2 The motion of a magnetic moment around the magnetic field and the resonance frequency

Key points
A magnetic moment rotates around the direction of the magnetic field $\vec{B}_o$ as does a spinning top. Its longitudinal component, along $\vec{B}_o$, is constant, whereas its transverse component, perpendicular to $\vec{B}_o$, rotates at the frequency F_o. F_o is proportional to the magnetic field intensity $\vec{B}_o$ and to the gyromagnetic factor characteristic of the nucleus, γ. The gyromagnetic factor γ has a characteristic value for each nucleus, so that at a given field value each kind of nucleus rotates at a specific frequency.

A magnetic moment $\vec{\mu}$ in presence of a magnetic field $\vec{B}_o$ is submitted to a torque: It rotates along a cone around the direction of the magnetic field, as does a spinning top. This special rotation is named precession (it is the name for the motion of a gyroscope when a torque is applied upon it). Then the longitudinal component of $\vec{\mu}$, μz, along $\vec{B}_o$, keeps a constant value, and the transverse component, μt, perpendicular to $\vec{B}_o$, rotates (Figure 1.2.2). The precession takes place at a well-defined frequency, F_o, proportional to the magnetic field intensity B_o and to the gyromagnetic factor, γ, characteristic of the nucleus.

F_o is the resonance frequency of this nucleus:

$$F_o = \gamma/2\pi . B_o \qquad (1.2)$$

The gyromagnetic factor γ is determined by the internal quantum structure of the nucleus. It has a characteristic value for each nucleus, so that at a given field value each kind of nucleus rotates at a specific frequency as shown in Table 1.2.1.

Figure 1.2.1 The hydrogen nuclear magnetic moment. The proton, with mass rotating upon itself, has some analogy with a spinning top. The positive charge rotating can also be described as some current flowing in a circuit and then behaves as a small magnet. Rotation (spin) is symbolized by the black arrow, magnetic moment by the grey arrow. The magnetic moment $\vec{\mu}$ and the spin $\vec{S}$ of a proton are collinear, and they are related by: $\vec{\mu} = \gamma.\vec{S}$, where γ is the gyromagnetic factor

Figure 1.2.2 Precession of a magnetic moment around the magnetic field. The magnetic moment of a proton rotates around the field $\vec{B_0}$ tangentially to a cone. The angle between $\vec{\mu}$ and $\vec{B_0}$ is constant; the projection of $\vec{\mu}$ on the direction of $\vec{B_0}$, μz – named the longitudinal component, has a fixed value. The projection upon the plane perpendicular to $\vec{B_0}$, $\vec{\mu t}$ – named the transverse component, rotates at the frequency F_0

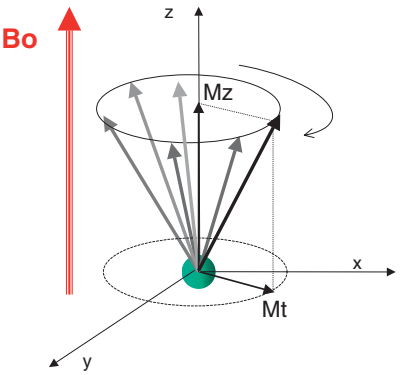

1.2.3 Resonance frequencies of nuclei of biological research

Amongst the stable nuclei, the hydrogen nucleus has the highest gyromagnetic factor and then the highest resonance frequency at a given magnetic field. NMR signals of hydrogen are currently detected at frequencies between 64 and 900 MHz (corresponding to magnetic field intensity between 1.5 T and 21.13 T). Other nuclei resonate at lower frequencies, because they have lower magnetic moments. These resonance frequencies are in the range used for radio, telephones and radars. In Table 1.2.1, the gyromagnetic factor γ of nuclei is expressed by their resonance frequency at $B_o = 4.7$ T (the field of many NMR spectrometers used for small animal examinations).

Table 1.2.1 Nuclear magnetic resonance frequencies at Bo = 4.7 Tesla for nuclei of biological interest

Nucleus	Frequency at 4.7 Tesla (MHz)	Natural abundance (%)	Sensitivity*
^{1}H	200	99.98	1
^{3}He	152.4	$1.3 \cdot 10^{-4}$	6.10^{-5}**
^{13}C	50.2	1.1	$0.18 \cdot 10^{-3}$
^{19}F	188.2	100	0.85
^{23}Na	52.9	100	0.136
^{31}P	80.9	100	0.063

*The sensitivity for a given nucleus is the ratio of its signal to the signal of hydrogen, at same number of atoms (taking into account the natural abundance of the isotope detected), at the same magnetic field. The sensitivity for ^{13}C is low because ^{13}C nuclei are only 1.1% of all carbon nuclei. The sensitivity varies as the square of the gyromagnetic ratio of the nucleus.

**This nucleus is detected at abundance higher than its weak natural abundance, after separation from ^{4}He, and after hyperpolarization (cf paragraph 1.10.1).

1.2.4 The nuclear magnetization

Key points
Nuclear magnetization is the sum of the individual magnetic moments per unit volume.

In presence of the external magnetic field B_o, individual magnetic moments are lined either parallel or anti-parallel to B_o, corresponding to two energy levels. The weak difference between the populations in these two energy levels determines the nuclear magnetization. At equilibrium, the nuclear magnetization is parallel to B_o, and its value M_o is proportional to the number of nuclei N and to B_o.

The magnetization is the sum of the individual magnetic moments in one unity of volume. These magnetic moments are borne by nuclei and electrons.

Here we consider only the magnetization from the nuclei, that we call 'nuclear magnetization', and only the contribution from the nuclei to be detected (very often hydrogen nuclei).

Let us consider a water sample of volume V that contains N hydrogen nuclei. In the absence of external magnetic field, the individual nuclear magnetic moments are oriented randomly with zero sum, and then the total magnetization is equal to zero (Figure 1.2.3(a)).

In the magnetic field $\vec{B}_o$, they do not behave as a classic magnet: A compass needle would always align with the field. Here they orientate either along or opposite the magnetic field (Figure 1.2.3(b)). Their z-component μz is quantified, taking values $+\mu$ or $-\mu$.

The magnetic energy of a magnetic moment $\vec{\mu}$ in the field $\vec{B}_o$ is given by

$$E = -\vec{\mu}.\vec{B}_o \qquad (1.3)$$

The two orientations relative to B_o determine two energy levels. The energy of the lower level is $E^+ = -\mu.B_o$, for $\vec{\mu}$ parallel to $\vec{B}_o$ (assuming μ is positive).

The energy of the upper level is $E^- = +\mu.B_o$, for $\vec{\mu}$ in the direction opposite to B_o.

The two levels are separated by

$$\Delta E = 2.\mu.B_o \qquad (1.4)$$

If the N hydrogen nuclei were reparted equally between these two levels, magnetization would still be zero. From thermal agitation, the hydrogen nuclei are continually jumping from one energy level to the other. At equilibrium, N^+ nuclei are in the lower level (which is slightly more populated) and N^- nuclei are in the upper level as drawn in Figure 1.2.4.

The magnetization, the sum of individual moments, is parallel to the magnetic field $\vec{B}_o$, and has the value M_o:

$$M_o = (N^+ - N^-).\mu/V \qquad (1.5)$$

This magnetization is much lower than $N.\mu/V$, which would be its value if all magnetic moments were in the lowest energy level. The magnetization at equilibrium

Figure 1.2.3 Nuclear magnetic moments and magnetization. The sum of the elementary magnetic moments in a unit volume is the magnetization. (a) At zero magnetic field, the magnetic moments are randomly oriented. (b) At the magnetic field intensity B_o, the magnetic moments are oriented either parallel or anti-parallel to $\vec{B}_o$ and their sum is parallel to $\vec{B}_o$

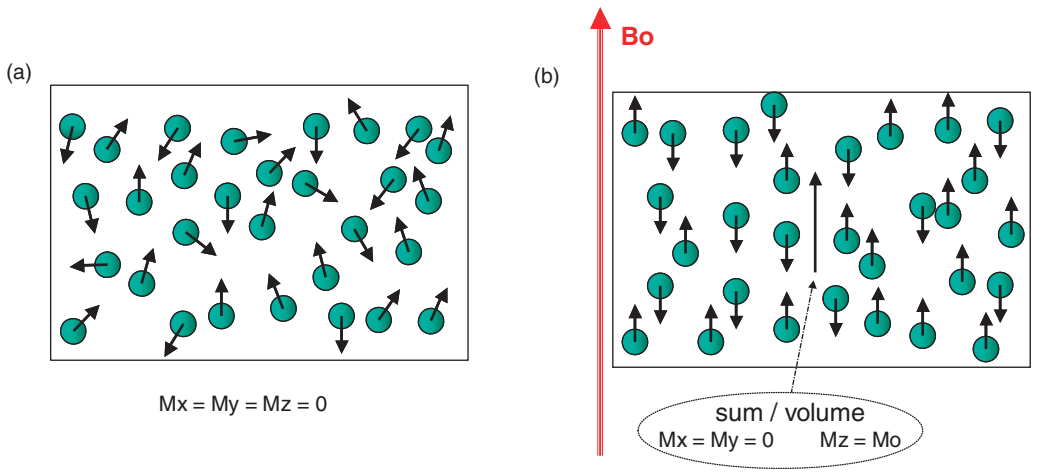

Figure 1.2.4 Population of the nuclear energy levels.
(a) Magnetic moments at equilibrium in the magnetic field B_o. The energy levels corresponding to the two orientations relative to B_o are separated by $\Delta E = 2\ \mu\ B_o$. The lower level contains N^+ hydrogen nuclei; the upper level contains N^- hydrogen nuclei. The net magnetization of the sample is $M_o = (N^+ - N^-)\ \mu/V$.
(b) Excitation of nuclear magnetic resonance. Photons from the electromagnetic field B_1, that have the energy $h\ F_o = \Delta E$, are absorbed and allow magnetic moments in the lower level to reach the upper level: The populations N^+ and N^- are modified by the absorption of photons. When $N^+ = N^-$ the longitudinal magnetization is equal to zero, while the photons have brought their polarization to the transverse magnetization that is no longer equal to zero.
(c) Energy levels and longitudinal relaxation. The recovery of M_z to equilibrium, or longitudinal relaxation, derives from rebuilding the difference between the populations N^+ and N^- of the two energy levels of hydrogen nuclei magnetic moments. The hydrogen nuclei that have been previously excited to the upper level have to emit the excess of energy in order to return to the lower level

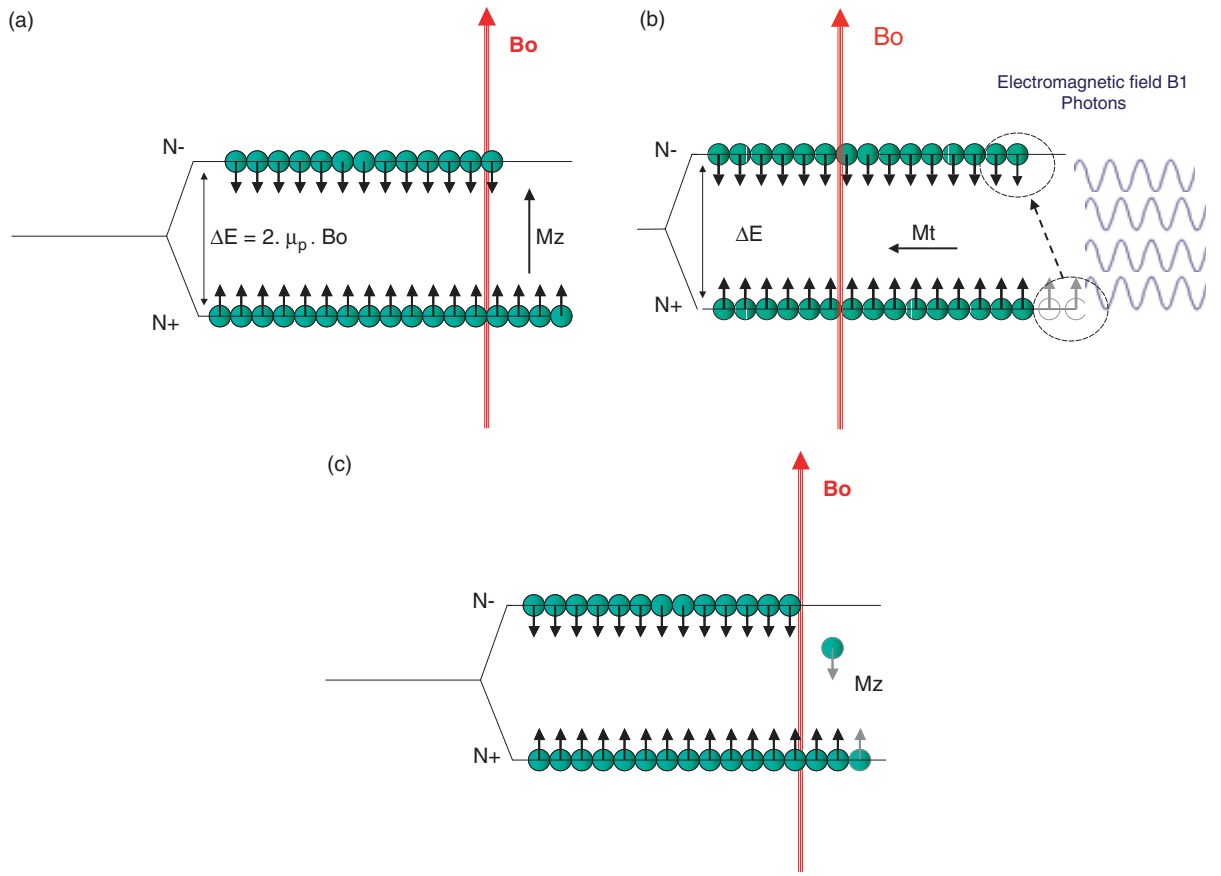

is calculated from the polarization P of nuclei that quantifies how much the magnetic moments are oriented by the magnetic field.

The polarization of nuclei by the magnetic field B_o, P is the ratio between the difference of populations of the two energy levels, $\Delta N = N^+ - N$, and the total population of nuclei, $N = N^+ + N^-$

$$P = \Delta N/N, \quad \text{so that } M_o = N\ P\mu/V. \tag{1.6}$$

At equilibrium, P depends on the ratio of the magnetic energy μBo (the source of magnetic order) to the thermal energy k T (the source of disorder), where k is the Boltzman constant and T the temperature.

This ratio is very low in usual in vivo conditions. The polarization of hydrogen nuclei is equal to 3×10^{-6} at 1 T, at 300°K. We shall later see that the signal from nuclei is related to the polarization. A benefit of stronger magnetic field is the higher polarization of nuclear magnetic moments. Special

Figure 1.2.5 Nuclear magnetization precesses around the magnetic field.
(a) At equilibrium, all individual magnetic moments experience precession around B_o at the frequency F_o. The individual magnetic moments are distributed randomly across each cone. The upper cone (corresponding to the lower energy level) is more populated than the lower cone: there is a net longitudinal magnetization, $M_z = M_o$. The transverse components of the magnetic moments rotate; their rotations are not coherent, so that there is no net sum along the other directions. Then for the nuclear magnetization of the sample $M_x = M_y = 0$.
(b) When the absorption of photons from the RF field B_1 has equalized the populations of the two cones and has modified the transverse orientations of the magnetic moments, $M_z = 0$ and M_t gets a net value (M_x and $M_y \neq 0$)

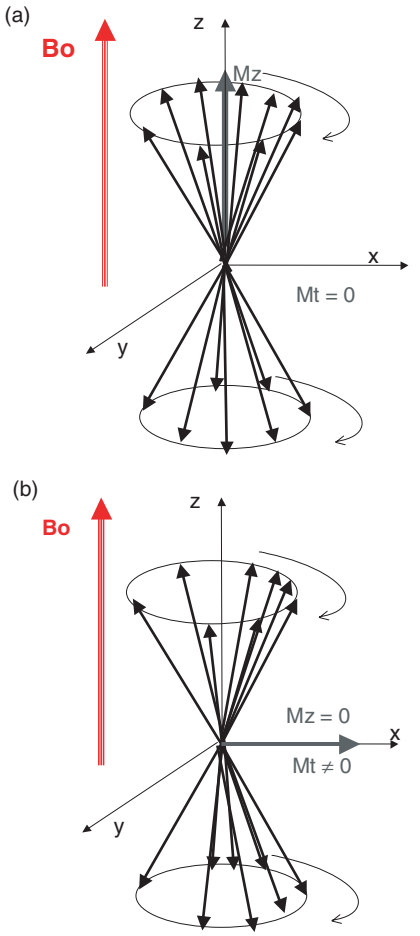

techniques allow to increase very strongly the polarization of nuclei such as Xenon, Helium and Hydrogen (see paragraph 1.10.1).

Let us come back to our small water sample and complete the description of magnetic moments.

At equilibrium, all the individual magnetic moments experience precession around B_o at the frequency F_o as displayed by Figure 1.2.2, but their transverse components are reparted randomly in the plane perpendicular to B_o and the sum of transverse components, M_t, is equal to zero (Figure 1.2.5(a)). After excitation of nuclear magnetic resonance, their transverse components are oriented in the plane perpendicular to B_o and the sum of transverse components, M_t, can be detected (Figure 1.2.5(b)).

1.3 Excitation and return to equilibrium of nuclear magnetization

Key points
Excitation of NMR is done by irradiation of the sample with a magnetic field oscillating at the resonance frequency F_o. This magnetic field tips the nuclear magnetization away from its initial orientation along B_o. While the transverse nuclear magnetization M_t rotates, it can be easily detected. The receiver probe picks the weak magnetic signal created by the rotation of M_t and generates a voltage oscillating at the frequency F_o. Detection can be done during a time limited by the decay of M_t, measured by the transverse relaxation time T2. One has to wait for the return to equilibrium of the longitudinal nuclear magnetization, during a time related to the longitudinal relaxation time T1, before repeating excitation and detection.

The magnetization at equilibrium, parallel to B_o, cannot be measured directly: Magnetic forces are small and difficult to measure. Conversely, when the global magnetization rotates around B_o at the resonance frequency, measurement of an electrical signal is possible.

Here we describe how to excite resonance, how to detect NMR signal, and the way nuclear magnetization returns to its initial equilibrium.

An oscillating or rotating physical phenomenon can be described by its amplitude, its frequency and its phase.

Both the RF magnetic field B_1 and the transverse magnetization M_t are vectors perpendicular to B_o that rotate or oscillate at the resonance frequency F_o (for definition of phase, see Figure 1.3.1).

At best, the field B_1 used for NMR excitation is a rotating field; however, the experiment is often driven

Figure 1.3.1 Oscillating/rotating vectors. The rotating vector M rotates in the plane XOY, as the needle of a clock; Ma, the amplitude of M is like the length of the needle. The angle of this vector with the reference axis OX is the phase ϕ. The rotation takes place at the frequency F (measured in turns per second or hertz). The phase at time zero is ϕ_o; later at time t the phase is written as

$$\phi = 2\,\pi\,F\,t + \phi_o. \qquad (1.7)$$

The components of the vector M are

$$M_x = M_a \cos(\phi) = M_a \cos(2\,\pi Ft + \phi_o), \qquad (1.8)$$
$$M_y = M_a \sin(\phi) = M_a \sin(2\,\pi Ft + \phi_o), \qquad (1.9)$$

M_x is an oscillating quantity, also characterized by its amplitude M_a, its frequency of oscillation F and its phase at $t = 0$, ϕ_o

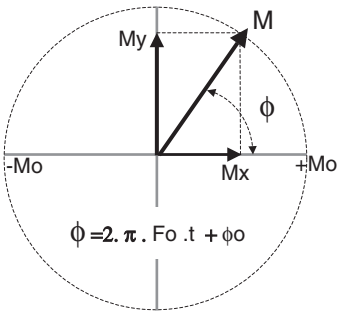

by a linear oscillating magnetic field that can be discomposed into two rotating fields: One of them rotates clockwise and the other counterclockwise. One of them is efficient to excite nuclear magnetic resonance and the other is not efficient.

The three characteristics of the transverse magnetization M_t are its amplitude, its precession frequency and its phase. They intervene in the generation of the NMR signal: The intensity of signal is proportional to the amplitude of the local magnetization, whereas the frequency and phase of the signal inform upon the spatial localization.

1.3.1 The excitation of nuclear magnetic resonance

To excite nuclear resonance means to set nuclear magnetization out of equilibrium by using a second magnetic field, the RF magnetic field $\vec{B_1}$ (RF means 'radio frequency'). This is done by irradiating the sample with an electromagnetic field rotating at the resonance frequency F_o. This field is created by sending current oscillating at the frequency F_o in a coil around the sample. (Note that this irradiation by an electromagnetic field is usually fully devoid of biological effects, except the thermal effects due to heating, because the energy of photons is more than 1×10^6 times smaller than any energy of ionisation: At the highest field used for MRI, 17.6 T, the photons of frequency 748 MHz have an energy equal to 3×10^{-6} eV. These photons can only heat tissues.)

The RF magnetic field $\vec{B_1}$ is perpendicular to $\vec{B_o}$ and rotates around the direction of $\vec{B_o}$. From the equivalence between electromagnetic field and photons, here again, there are two complementary descriptions of the excitation of resonance.

1.3.1.1 In terms of energy levels and populations

An electromagnetic wave of frequency F can also be described as made by photons of elementary energy

$E = h\,F$ (where h is the Planck's constant equal to 6.634×10^{-27} J.s).

The RF magnetic field $\vec{B_1}$ at the resonance frequency F_o is the magnetic component of an electromagnetic wave. The energy of the corresponding photons, equal to $h\,F_o$, is exactly equal to the difference between the magnetic energy of magnetic moments in the two energy levels, $\Delta E = 2\,\mu\,B_o$. Such photons convey exactly the energy needed to raise one magnetic moment from the lower level up to the higher level, whence the name of resonance frequency (Figure 1.2.4(b)).

When the two populations get equal, M_z is equal to zero and $M_t = M_o$. This is described geometrically as a 90° flip of the vector $\vec{M}$ that rotates around the direction of the RF field $\vec{B_1}$ (Figure 1.3.2).

The photons of the electromagnetic field at frequency F_o are fully polarized: This means that for every photon, the direction and phase of $\vec{B_1}$ is well defined and identical. When the photons are absorbed by the magnetic moments they give a well-defined value to the transverse component of the elementary magnetic moments, so that the transverse magnetization is no more equal to zero.

1.3.1.2 In terms of vectors and forces

The magnetic field $\vec{B_1}$ is perpendicular to $\vec{M}$ and exerts a force upon it. Under this force, the orientation of $\vec{M}$ is modified: $\vec{M}$ is tipped away the z axis.

Figure 1.3.2 Flip of the magnetization induced by the RF magnetic field B_1. The magnetic field B_1, perpendicular to the magnetization M and to B_o, exerts a torque upon M and modifies its direction. Since B_1 rotates around B_o at the same frequency F_o than does M, it keeps an adequate angle with M during the precession, and its action goes on during the rotation of M. Note that this drawing does not shows the fast rotation of M and B_1 at the frequency F_o: The observer is 'in the rotating frame' that rotates at the frequency F_o. Many of the following graphs are drawn with the same convention

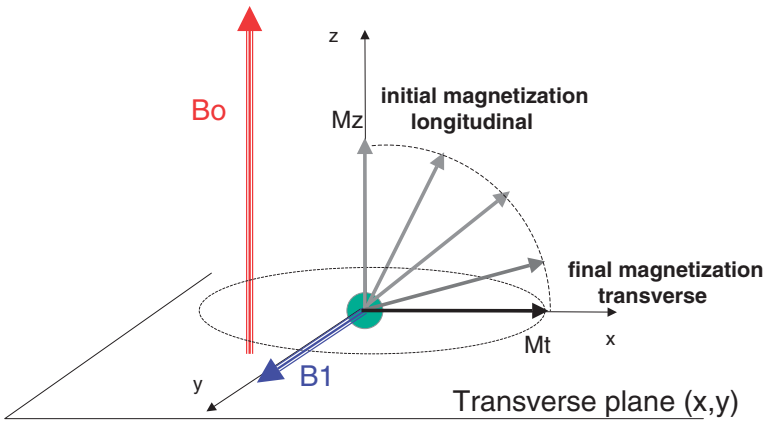

Both $\vec{M}$ and $\vec{B_1}$ rotate at the frequency F_o: The force exerted by $\vec{B_1}$ upon $\vec{M}$ also rotates, so that $\vec{M}$ goes on tipping away from z axis, and, while continuing its precession around $\vec{B_o}$, rotates around $\vec{B_1}$ (Figure 1.3.2).

The angulation of $\vec{M}$ relative to $\vec{B_o}$, induced by application of the RF field $\vec{B_1}$, is measured by the angle between the two vectors and is named as the flip angle. The magnitude of the flip angle depends on the amplitude of B_1 and the duration of its application τ, and also on the gyromagnetic factor γ, according to the relation

$$\alpha = \gamma B_1 \tau. \qquad (1.10)$$

When the flip angle reaches 90°, so that $\vec{M}$ is perpendicular to $\vec{B_o}$, the RF field $\vec{B_1}$ is shut down. Now the magnetization is fully 'transverse': The vector $\vec{M}$ lies in the plane x-y and rotates around $\vec{B_o}$ at the frequency F_o. The transverse component M_t is the largest possible at the end of a 90° flip: Then M_t is equal to the value of M_z before the application of $\vec{B_1}$ and $M_z = 0$.

The sample is ready for detection of the rotating transverse nuclear magnetization.

Usually B_1 is applied during a very short time, at high intensity: This is called a pulse of RF magnetic field. The RF pulse, which makes a 90° flip angle, is called a '90° RF pulse'.

Other trajectories are possible with a flip angle smaller than 90° (M_z is smaller but positive at the end of the RF pulse) or larger than 90° (M_z is negative at the end of the RF pulse).

More physics: the 180° RF pulse.
Initially, the nuclear magnetization is at equilibrium ($M_z = M_o$) corresponding to the difference ΔN between the populations N^+ and N^-. After irradiation by the RF field B_1 at the resonance frequency, when the number of photons absorbed by the nuclear magnetic moments is twice of that corresponding to a 90° pulse, the difference between populations N^+ and N^- is inverted: The upper level is more populated and the longitudinal magnetization has the value $-M_o$. Magnetization has been inverted; geometrically, this corresponds to a flip angle of 180° around the direction of B_1.

A 180° RF pulse is also applied in order to refocus the transverse magnetization and hence to generate a spin echo (see Section 1.3.4). Then its effect is to invert the component of M_t perpendicular to the RF field B_1 as shown in Figure 1.3.3(b).

1.3.2 How to detect the nuclear magnetization?

Nuclear magnetization can be detected while it rotates at a well-defined frequency after excitation. Voltage at the same frequency is induced in a receiver coil.

When a magnet bar rotates next to a loop of conducting wire, a voltage is induced and current flows in the loop. The simplest receiver coil is a loop of conductive wire designed to deliver a large voltage when it 'sees' a small magnetic field oscillating at the frequency F_o.

Let us consider a small sample containing water, in proximity to the receiver coil. After excitation of NMR